ELSEVIER Science Press
Available online at www.sciencedirect.com
ScienceDirect
Trans. Nonferrous Met. Soc. China 32(2022) 3563−3577
Transactions of Nonferrous Metals Society of China
www.tnmsc.cn

Influence of free-end torsion on compressive behavior of extruded AZ31 rod at various temperatures

Fan WU, Meng WANG, Zhi-wen DU, Ruo-lan SHI, Qi SHANG,
Ting-ting LIU, Ning GUO, Sheng-feng GUO, Bo SONG

School of Materials and Energy, Southwest University, Chongqing 400715, China

Received 7 September 2021; accepted 25 February 2022

Abstract: The influence of free-end torsion on compressive behavior of an extruded AZ31 rod at various temperatures was studied. Pre-torsion generates a high density of dislocations and a large number of $\{10\bar{1}2\}$ twins in the matrix, which can largely enhance the compressive yield strength at RT and 100 °C. However, with increasing temperature, hardening effect via pre-torsion gradually decreases. When the compressive temperature reaches 300 °C, pre-torsion reduces the compressive yield strength. Moreover, initial dislocations and twins via torsion help to refine the sub-structure and accelerate the continuous dynamic recrystallization during compression at 200 °C. Thus, twisted sample exhibits more rapid flow softening behavior than the as-extruded sample at 200 °C. When compressed at 300 °C, the twins and dislocations via torsion were largely eliminated during the holding time, and the discontinuous dynamic recrystallization was enhanced. It is found that the compression curves of twisted sample and as-extruded sample tended to be coincident at 300 °C. Related mechanisms were discussed in detail.

Key words: Mg alloys; free-end torsion; compressive behavior; dynamic recrystallization; hot deformation; twins; dislocations

1 Introduction

Mg and its alloys are receiving more and more attention due to their low density. They have the opportunity to manufacture lightweight components for the automotive, aerospace and communication industries. However, their poor mechanical properties limit their widespread use. Plastic processing (e.g. rolling, extrusion, and forging etc.) has been used to improve the mechanical properties of Mg alloys by refining grains [1−4]. However, traditional plastic processing technologies usually exhibit limited refinement ability and generate strong wrought texture. Thus, in order to further refine grains and optimize texture, some new plastic processing technologies have been developed, e.g. asymmetry rolling/extrusion, equal channel angular extrusion, and cumulative rolling [1,5−7].

Recently, it has found that simple plastic deformation with low-cost (e.g. tension [8], compression [9], pre-rolling [10], shear [11], and free-end torsion [12,13]) can further optimize the microstructure of wrought Mg alloys. They can be the important supplement to traditional plastic processing technologies. Among them, free-end torsion can generate gradient microstructure and can achieve a large plastic strain [12,14,15]. Because of these advantages, free-end torsion has received widespread attention. Previous work has found that free-end torsion at room temperature can introduce high-density dislocations and $\{10\bar{1}2\}$ twins, and can also arouse large textural change in Mg alloys [14]. According to previous reports, pre-torsion deformation has been successfully applied to improving the strength, anisotropy, and

---

Corresponding author: Bo SONG, Tel: +86-23-68253204, E-mail: bosong@swu.edu.cn

DOI: 10.1016/S1003-6326(22)66039-4

toughness of Mg alloys [14,16,17]. Especially, remarkably high compressive yield strength can be obtained in twisted AZ31 rod [12]. However, previous publications were largely limited to the investigation of mechanical properties at room temperature. With increasing temperatures, the balance of the various deformation modes will change [18,19]. Moreover, dynamic recrystallization (DRX) can occur to influence deformation behavior during hot deformation [20−24]. However, there is no report to investigate the influences of pre-torsion on hot deformation behavior and DRX behavior. In this work, free-end torsion was performed to process the extruded AZ31 rod. Compressive deformation behavior at different temperatures was analyzed. Plastic deformation mechanism and DRX mechanism were discussed.

2 Experimental

An extruded AZ31 rod (Mg−3wt.%Al−1wt.%Zn) with a diameter of 16 mm was used as the initial material which was marked as AE sample. The dog-bone-shaped torsion samples with a gauge section of 70 mm (length) × 10 mm (diameter) were cut from the extruded bar. The free-end torsion test was performed by a torsion machine (NDW30500, Changchun Ke Xin instrument, China) at a speed of 1 r/min. The AE sample has an ultimate torsion angle of about 270° at room temperature (RT). Here, the extruded rod was designed to twist 250° at RT, resulting in a shear strain of ~0.31 at the edge position of pre-torsion sample. The shear strain can be calculated as $\gamma=2\pi Nr/l$, where γ is the shear strain, N is the number of rotation, r is the radial position in the sample, and l is the sample length. Pre-torsion sample is marked as the PT sample.

The nominal size samples with 10 mm (diameter) × 6 mm (length) were cut from the twisted rod and extruded rod for the compression test. The compression test along the ED was carried out at RT, 100, 200, and 300 °C on a LD26.105 material test machine (LiShi (Shanghai) Instruments Co., Ltd., China). Before hot compression, the samples were held at compression temperature for 10 min in a resistance furnace. The compression rate was $1\times10^{-3}\ \mathrm{s}^{-1}$. Each mechanical test was repeated at least three times to get representative results. Microstructures of samples compressed at different temperatures to various strain levels (5%, 15% and 50%) were characterized using optical microscopy and electron backscatter diffraction (EBSD, NordlysMax3 equipped, Oxford Instruments, London, UK). Torsion deformation induces the largest change in microstructure at the edge position on the cross-section of sample [14]. Thus, the edge position on the cross-section of the sample is characterized to investigate the effect of torsion on microstructure evolution. In this work, the name of the compressed sample is marked according to the following rules: sample state-deformation temperature-plastic strain. For example, the AE sample compressed by 15% at 200 °C is marked as AE-200 °C-15% sample.

3 Results and discussion

3.1 Effect of free-end torsion on microstructure

Figure 1(a) shows the basal pole figure and EBSD maps of the AE sample. The AE sample has a recrystallized microstructure. The average grain size is about 25 μm. However, the recrystallized microstructure exhibits a wide range of grain-size distribution from 2 to 50 μm. The {0001} pole figure shows that the extruded rod exhibits a typical extrusion fiber texture. In other words, the *c*-axis of most grains is perpendicular to the ED direction.

Figure 1(b) shows the basal pole figure and EBSD maps of the edge position with maximum shear strain (~31%) in the PT sample. Torsion deformation can introduce profuse $\{10\bar{1}2\}$ twins, which can cause a large re-orientation of the lattice (~86.3°) [25,26]. Thus, $\{10\bar{1}2\}$ twins can generate a new texture component (see the T-ori. in Fig. 1(b)). The *c*-axis of twin-texture is located at ~40° from the ED, and thus is named as 40-ED texture. Dislocation slips activated during torsion deformation can also cause the *c*-axes of parent grains to rotate towards the ED [27]. For the edge position of the PT sample, the basal pole peak of parent grains is located at ~70° from the ED (named as 70-ED texture). Besides change of texture, torsion also introduces profuse dislocations and twins in the matrix, as shown in Fig. 1(b). Kernel average misorientation (KAM) map is measured to estimate the distribution of dislocations [28]. Torsion deformation largely increases the average KAM value from 0.41° (in AE sample) to 1.77° (at the edge position of the PT sample). Based on the EBSD data, area fraction of twins can also be

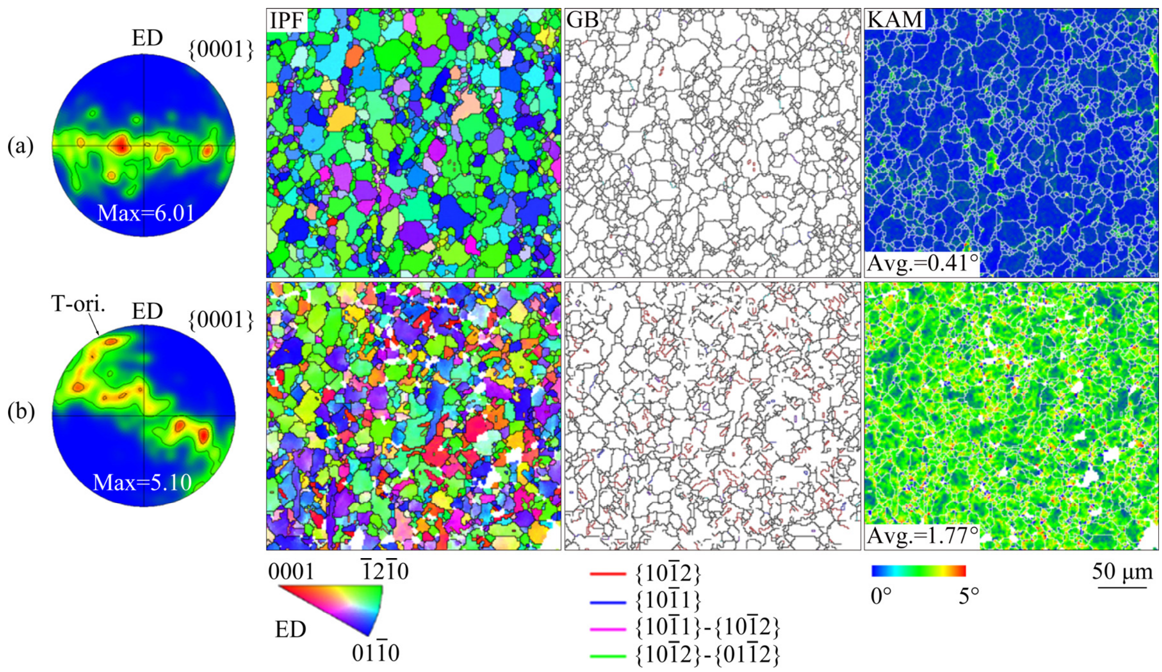

Fig. 1 {0001} pole figures, inverse pole figure (IPF) images, grain boundaries (GB) images and KAM images of various samples: (a) AE sample; (b) Edge position of PT sample

calculated. According to the orientation analysis, twins and parent grains can be identified. The twins can be extracted from the matrix by Channel 5 software to obtain the area fraction of twins. The area fraction of twins is also calculated as 28% at the edge position of the PT sample.

3.2 Mechanical properties and yield behavior

Figure 2 shows the true compressive stress−strain curves of various samples at different temperatures. Detail mechanical properties are listed in Table 1. Torsion deformation has a great influence on the compressive behavior at less than 200 °C. For low-temperature compression (≤200 °C), torsion deformation significantly increases the compressive yield strength. As compression temperature increases, the increment of yield strength gradually decreases. The increment of yield strength is 52 and 40 MPa for compression at RT and 100 °C, respectively. With increasing compression temperature to 200 °C, the increment is reduced to 7 MPa. When compressed at 300 °C, torsion deformation reduces (by 14 MPa) the yield strength of the extruded rod.

In order to reveal the yield behavior, the microstructure at the initial stage of plastic deformation (5% plastic strain) is characterized by EBSD. In this work, the microstructure at the edge position of the rod is used to discuss the influence of torsion on the microstructure evolution and deformation mechanism. Figure 3 shows the microstructure of the AE and PT samples compressed by 5% at various temperatures. After being compressed by 5% at RT and 100 °C, a large number of $\{10\bar{1}2\}$ twins can be found in AE sample (see Figs. 3(a) and (c)). It indicates that $\{10\bar{1}2\}$ twinning dominates the initial strain. In fact, the s-shaped flow curve (see Figs. 2(a) and (b)) is the characteristic of twinning-dominated deformation [29]. The area fraction of $\{10\bar{1}2\}$ twins (f_{twin}) can be obtained by EBSD data. It shows that the f_{twin} is 50% and 36% for AE-RT-5% sample and AE-100°C-5% sample, respectively. Here, the strain accommodated by $\{10\bar{1}2\}$ twinning ($\varepsilon_{\text{twin}}$) is estimated by a reported formula [30]: $\varepsilon_{\text{twin}}=f_{\text{twin}}\cdot m\cdot\gamma_{\text{twin}}$, where m is the Schmid factor for $\{10\bar{1}2\}$ twinning, and γ_{twin} represents the $\{10\bar{1}2\}$ twinning characteristic shear factor (~0.13). When the AE sample is compressed along the ED, the average Schmid factor of $\{10\bar{1}2\}$ twinning is close to 0.5. Thus, after being compressed by 5%, the contribution of twinning strain to total strain is 65% and 47% for AE-RT-5% sample and AE-100°C-5% sample, respectively. With increasing compression temperature, the contribution of $\{10\bar{1}2\}$ twinning to plastic strain rapidly reduces.

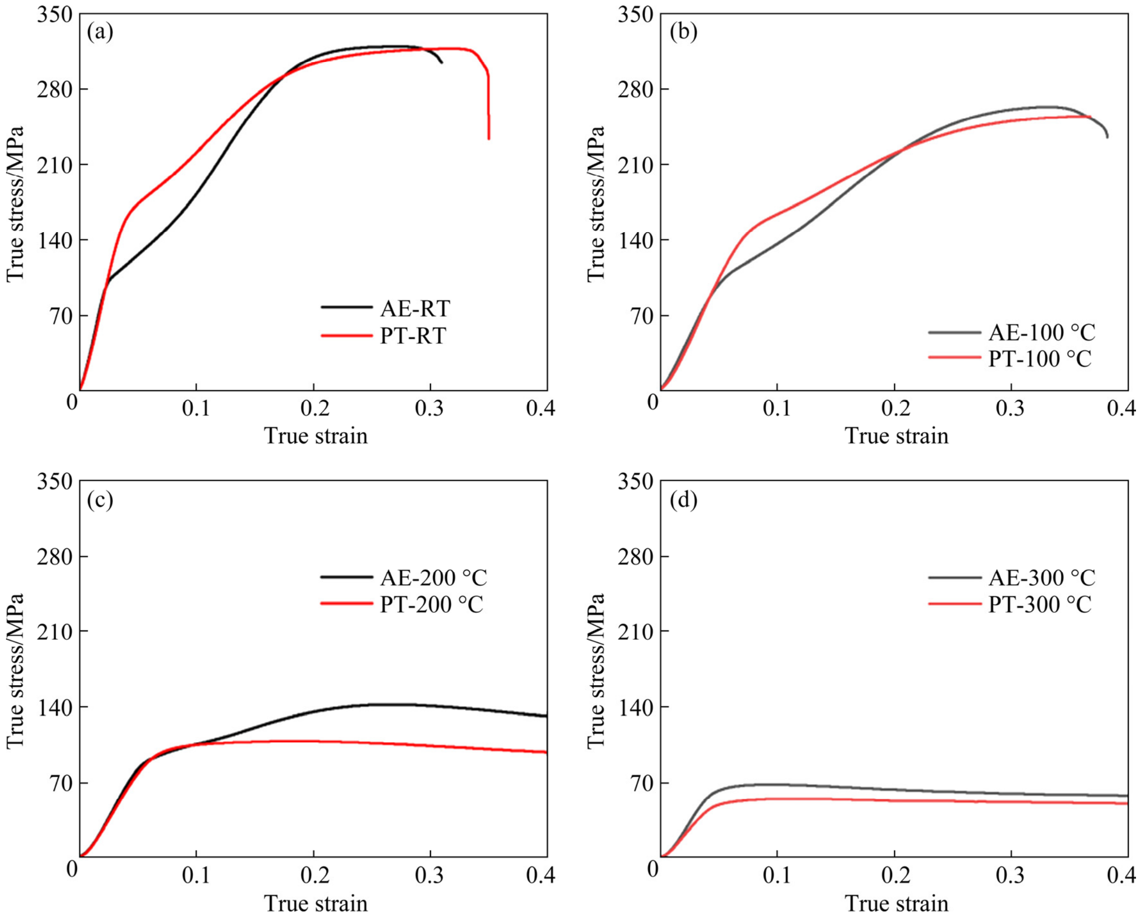

Fig. 2 True stress−strain curves of various samples under uniaxial compression at different temperatures: (a) RT; (b) 100 °C; (c) 200 °C, (d) 300 °C

Table 1 Yield strength (YS), peak strength (PS) and compression ratio (CR) of various samples

Temperature/°C	AE sample			PT sample		
	YS/MPa	PS/MPa	CR/%	YS/MPa	PS/MPa	CR/%
RT	101±5	319±2	28.1±0.5	153±5	317±2	33.5±0.4
100	96±7	262±3	36.3±0.3	136±5	254±5	35.1±0.3
200	85±3	141±2	−	92±5	108±2	−
300	62±3	67±3	−	48±5	53±2	−

In the AE-200°C-5% sample, the f_{twin} is only 4% (see Fig. 3(e)). For AE-300°C-5% sample, few twins were found in the matrix, as shown in Fig. 3(g). It indicates that as the compression temperature rises from RT to 300 °C, the dominant deformation mechanism is transformed from $\{10\bar{1}2\}$ twinning to slip.

The activation stresses of various deformation modes can be calculated by CRSS/SF (CRSS and SF represent critical resolved shear stress and Schmid factor, respectively). The effect of temperature on the dominant deformation mode is closely related to the temperature dependence of the CRSS values of different deformation modes. TAM et al [18] have studied the effect of temperature (from 25 to 200 °C) on CRSS values of slip and twinning in a rolled AZ31 alloy with an average grain size of 25 μm. Based on the result, the activation stress (CRSS/SF) of various deformation modes as the function of compression direction is drawn in Fig. 4. For the AE sample with extrusion fiber texture, the loading angle between *c*-axis of the texture and compressive axis is close to 90° (see Fig. 1(a)). In this situation, basal slip with the

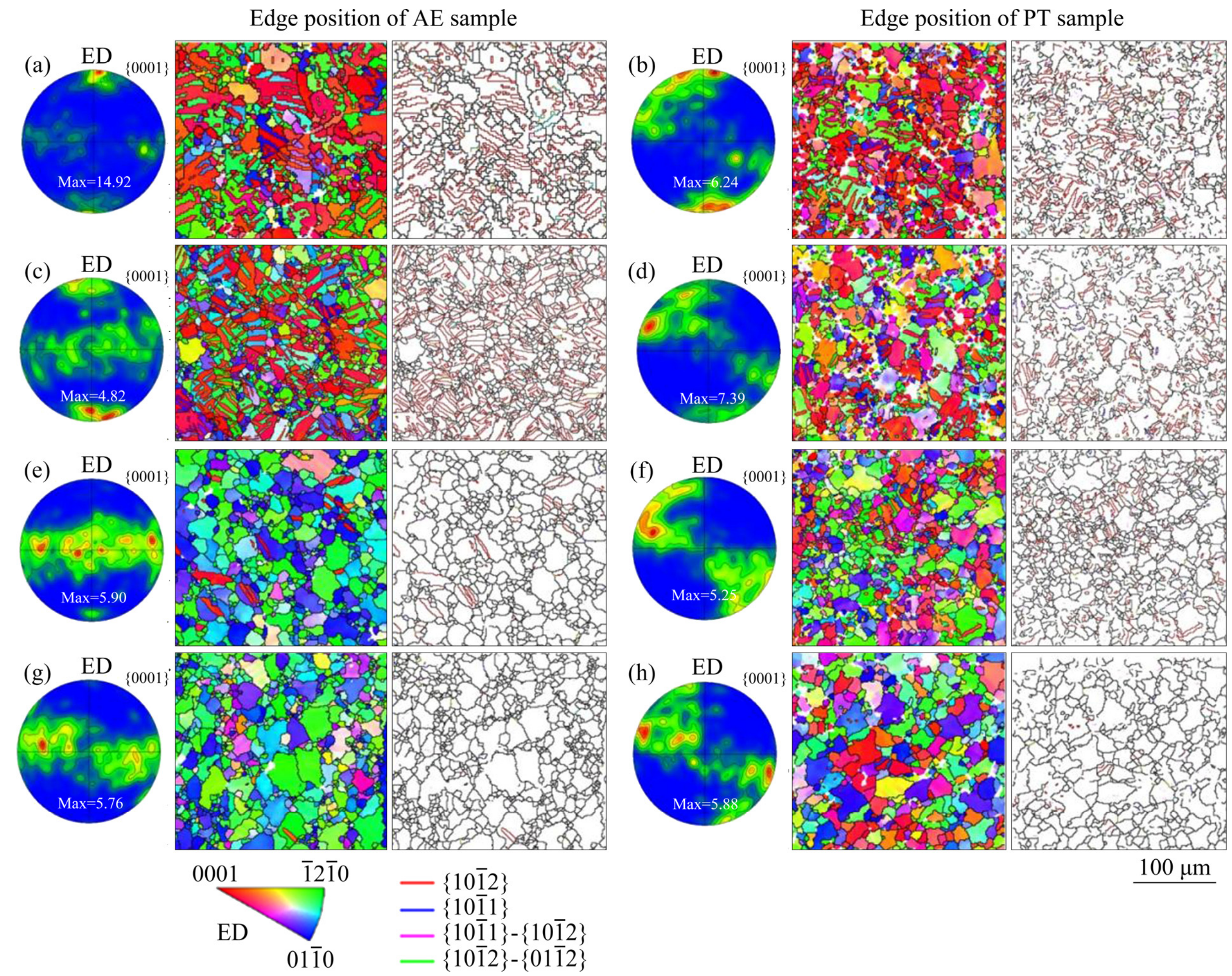

Fig. 3 EBSD maps and basal pole figures at edge positions of AE and PT samples compressed by 5% at various temperatures: (a, b) RT; (c, d) 100 °C; (e, f) 200 °C; (g, h) 300 °C

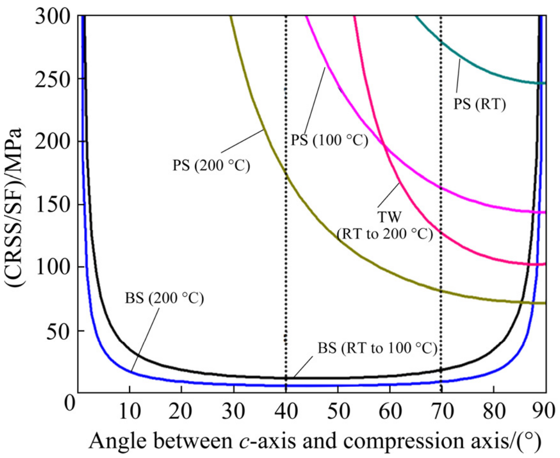

Fig. 4 Activation stress of various deformation modes at different temperatures (BS, PS and TW represent basal slip, prismatic slip and $\{10\bar{1}2\}$ twinning, respectively)

lowest CRSS is hard to activate owing to very low SF. Cleary, $\{10\bar{1}2\}$ twinning has the lowest activation stress for compression at less than 100 °C. Although CRSS of $\{10\bar{1}2\}$ twinning is not sensitive to temperature, the CRSS values of non-basal slip modes rapidly decrease with increasing temperature. As shown in Fig. 4, when compression temperature reaches 200 °C, the activation stress of prismatic slip is lower than that of $\{10\bar{1}2\}$ twinning. It is also reported that pyramidal $\langle c+a\rangle$ slip can also be activated at above 200 °C [18]. Thus, for the AE sample, as compression temperature rises, the dominant deformation mode of yield will change from $\{10\bar{1}2\}$ twinning to slip. Moreover, as the temperature increases, the decrease in the yield strength can also be attributed to the softening of non-basal slip.

For the PT sample, after being compressed by 5% at RT and 100 °C, the area fraction of newly generated twins during compression is only 18% and 3%, respectively (see Figs. 3(b) and (d)). It is indicated that pre-torsion largely reduces the contribution of twinning on plastic deformation. It can be attributed to textural change during torsion, as shown in Fig. 1. According to the result in Fig. 4, textural change via torsion will enhance the activation of basal slip. Figure 4 also indicates that enhancement of basal slip usually leads to a texture softening effect and reduces the yield strength [18]. However, torsion deformation largely enhances the compressive yield strength at RT and 100 °C. The increased yield strength at RT has been ascribed to the defects hardening effect via dislocations and twin-boundaries in the PT sample [31]. SONG et al [14] found that recrystallization annealing can reduce the compressive yield strength of the PT sample to a close level with the AE sample. For PT-100 °C sample, slight decrease in yield strength might be due to the dislocation recovery during the heat preservation process. With increasing temperature, static recovery and recrystallization occur more drastically. As the temperature increases to 200 °C, the yield strength of the PT sample dropped to a level close to that of the AE sample. After being compressed by 5% at 200 °C, the initial twins via pre-torsion can be retained in the initial stage of deformation, as shown in Fig. 3(f). It indicates that only static recovery occurred during heat preservation process at 200 °C. After being compressed by 5% at 300 °C, twin-orientation (i.e. 40-ED texture) is remained in PT-300 °C-5% sample. However, the area fraction of twin lamellae is largely reduced to 2%, as shown in Fig. 3(h). It infers that initial twins are eliminated by static recrystallization during the heat preservation process at 300 °C. Thus, the softening effect via static recrystallization plays a critical role in the decrease in yield strength with increasing temperature for the PT sample. As the compression temperature increases to 300 °C, the PT sample exhibits lower yield strength than the AE sample. It is considered that texture softening effect via torsion is the dominant factor for the low yield strength in the PT sample.

3.3 Strain hardening and softening behavior

Torsion deformation can also largely influence the flow behavior during compression, as shown in Fig. 2. Compressive strain hardening rate curves of various samples at different temperatures are shown in Fig. 5. For compression at RT and 100 °C, after elastic−plastic transition, a linearly increasing strain hardening rate stage with strain can be found (Stage II hardening). It is a typical feature of $\{10\bar{1}2\}$ twinning [29]. As shown in Fig. 3, $\{10\bar{1}2\}$ twins generated during compression have a *c*-axis//ED texture, which is a hard orientation for basal slip, $\{10\bar{1}2\}$ twinning and prismatic slip. The rapid increase in strain hardening rate is related to the texture hardening via lattice reorientation during twinning [29].

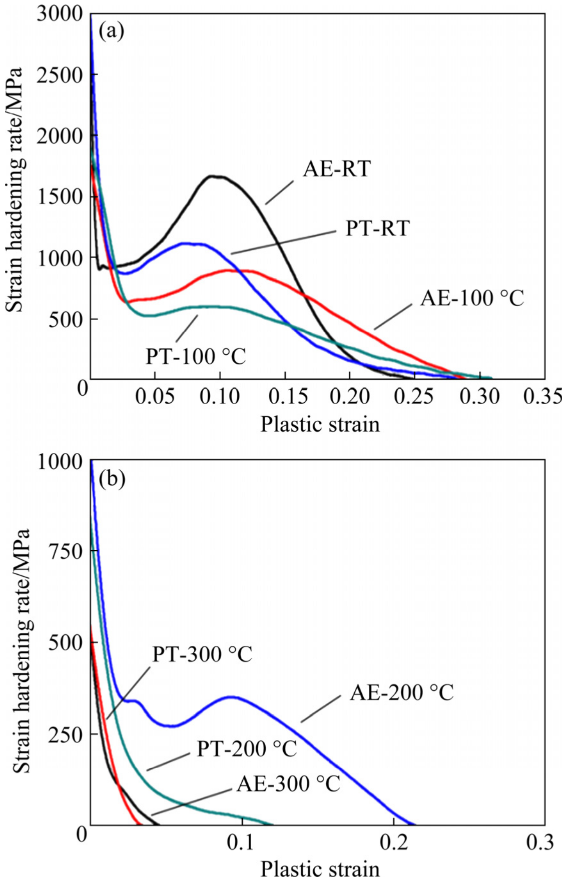

Fig. 5 Strain hardening rate vs plastic strain curves of compression at RT and 100 °C (a), and 200 and 300 °C (b)

Torsion deformation reduces the strain hardening rate of Stage II hardening and shortens the strain corresponding to Stage II hardening. It indicates that pre-torsion largely affects twinning behavior during subsequent compression. Three typical grains in the PT-100 °C-5% sample are analyzed to reveal the effect, as shown in Fig. 6. In the PT sample, some grains remain extrusion fiber texture (e.g. grain G1). For these grains, $\{10\bar{1}2\}$ twinning is still favorable for compression at RT and 100 °C. According to the orientation, it is inferred that T11 is the newly generated twin during

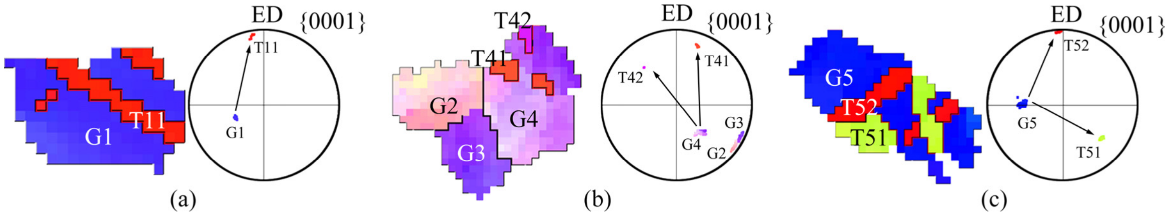

Fig. 6 Typical grains in PT-100 °C-5% sample: (a) Grain G1 without initial twins; (b) Grains G2−G4 with tilt extrusion texture; (c) Grain G5 with initial Twin T51 (G*i* and T*ij* (*i*, *j*=1, 2, 3, ⋯) represent the parent grain and twin lamellae, respectively)

compression. In fact, after torsion, most grains are re-oriented or twinned, as shown in Fig. 1. Texture change during torsion will influence the dominant deformation mode, as shown in Fig. 4. For the parent grains with 70-ED texture and initial twins with 40-ED texture, basal slip has far lower activation stress than $\{10\bar{1}2\}$ twinning. Thus, $\{10\bar{1}2\}$ twinning is not favorable during compression for the PT sample. As shown in Fig. 6(b), the parent grains with tilt extrusion texture are difficult to activate twinning (e.g. G2, G3 and G4) during compression. Even if the $\{10\bar{1}2\}$ twins are activated (e.g. G4), the size of the newly generated twins is very small. Initial twins via torsion can also influence the twinning behavior during compression. Figure 6(c) shows the twinning behavior of a typical grain with initial twins. According to the orientation, it is inferred that twin variant T51 is from torsion deformation and the twin variant T52 is the newly generated twin during compression. EBSD map indicates that the growth of T52 is strongly limited by the twin boundary of T51. It has been reported that the hardening effect of the initial twin boundaries on $\{10\bar{1}2\}$ twinning is higher than that on slip [32]. Thus, initial twins can largely limit the nucleation and growth of newly generated twins during compression. Clearly, both textural change and initial twins via torsion will reduce the contribution of twinning on strain. It is the reason why pre-torsion reduces the strain hardening rate of Stage II hardening [32].

As compression temperature rises, the strain corresponding to the Stage II hardening tends to decrease and eventually disappear, as shown in Fig. 5. This further proves that the dominant deformation mechanism is transformed from $\{10\bar{1}2\}$ twinning to slip with increasing temperature.

With the increasing strain at 200 °C, both the AE sample and the PT sample exhibit obvious flow softening behavior, as shown in Figs. 2(c) and Fig. 5(b). It is related with dynamic recovery and dynamic recrystallization during hot compression. Moreover, the PT sample shows more rapid flow softening behavior than the AE sample. For the AE sample, a high strain hardening can be remained to contribute an increase of stress (~40 MPa) at the beginning of plastic deformation at 200 °C. It might be related to the activation of limited twins, as shown in Fig. 3(e). When compressed at 300 °C, the flow curves of both samples tend to be coincident. The strain hardening rate curves at 300 °C exhibit more rapid decrease than those at 200 °C.

Optical micrographs of the edge positions in the samples compressed at 200 °C are shown in Fig. 7. When compressed to a strain of 15%, no obvious recrystallized grains were observed for both samples (Figs. 7(a) and (b)). However, some bulges of grain boundaries can be found (labeled by red arrows). It is a typical feature of discontinuous dynamic recrystallization (DDRX) [4]. With an increase of strain to 50%, profuse fine DRX grains are found in both samples. DRX grains usually generate surround the coarse-grain boundaries (Figs. 7(c) and (d)). Moreover, it is found that the amount of DRX grains in the PT-200 °C-50% sample is higher than that in the AE-200 °C-50% sample. It indicates that pre-torsion might accelerate DRX process. DRX process will generate a softening effect. It is inferred that the accelerated DRX process leads to more rapid compression flow softening feature in the PT sample, as indicated in Fig. 5(b).

Figure 8 shows the optical micrographs at the edge positions in the samples compressed at

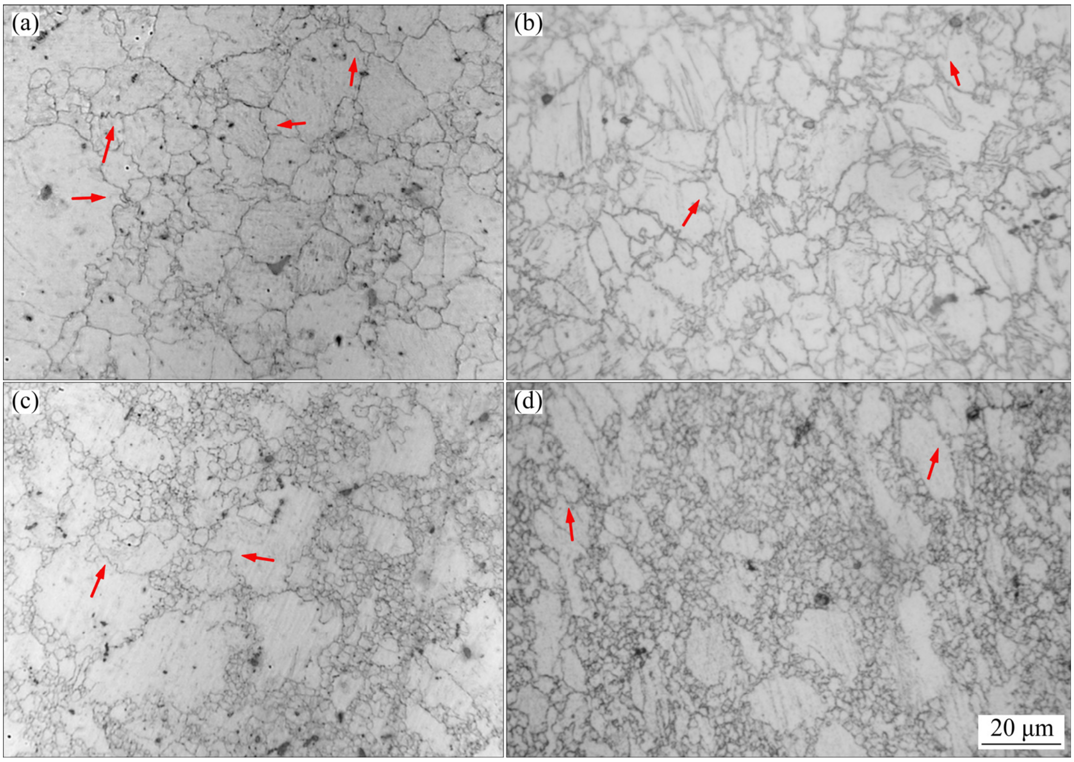

Fig. 7 Typical optical micrographs of various samples compressed at 200 °C to different strain levels: (a) AE-200 °C-15%; (b) PT-200 °C-15%; (c) AE-200 °C-50%; (d) PT-200 °C-50%

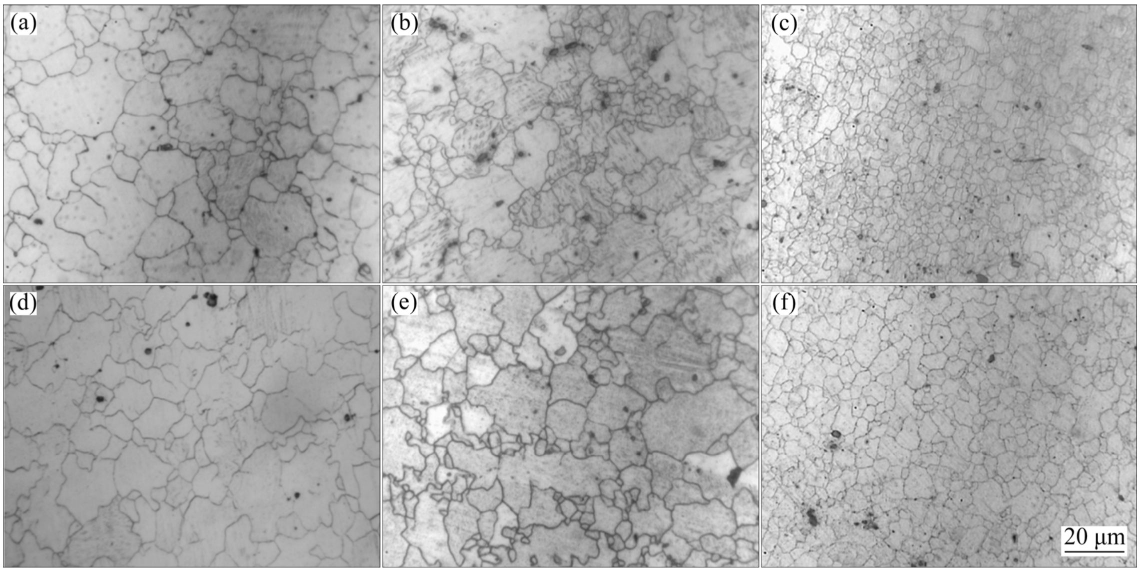

Fig. 8 Typical optical micrographs of various samples compressed at 300 °C to different strain levels: (a) AE-300 °C-5%; (b) AE-300 °C-15%; (c) AE-300 °C-50%; (d) PT-300 °C-5%; (e) PT-300 °C-15%; (f) PT-300 °C-50%

300 °C. After being compressed to a strain of 5%, both samples exhibit equiaxed microstructure without twins. This is consistent with the results of EBSD in Fig. 3. Compared with compression at 200 °C, compression at 300 °C generates more bulges of grain boundaries to induce dynamic recrystallization, as shown in Fig. 8. After being compressed by 50%, almost completely recrystallized structure can be obtained for both samples. Figure 8 also indicates that the AE and PT samples exhibit similar recrystallization process during compression at 300 °C. It might be the reason why the PT sample and the AE sample exhibit similar compression flow behavior at 300 °C.

3.4 DRX mechanisms

Figure 9 shows the EBSD data at the edge positions of the samples compressed to a strain of 15% at 200 °C. It is found that compression at 200 °C rotates the *c*-axis of texture towards the ED for both samples. Moreover, lots of low-angle grain boundaries (LAGBs) can be found in the compressed samples. Clusters of LAGBs within grain will cause the generation of sub-grains, which are considered as the infancy of DRX grains [33,34]. This is the formation process of continuous dynamic recrystallization (CDRX).

To further reveal the DRX mechanism, three typical grains in the AE-200 °C-15% sample are shown in Fig. 10. Figure 10(a) shows two grains without twins (G1 and G2). It indicates that only dislocation slip is activated to accommodate the compressive strain. The point-to-origin misorientation distribution along the black arrows in two grains is also shown in Fig. 10(a). It is found that the point-to-origin misorientation gradually increases to above 9°. It indicates that a large number of dislocation clusters and strong lattice distortion inside the initial grains occur during compression at 200 °C [35]. GB map indicates that LAGBs are formed with the change of misorientation within grains. Thus, for the AE sample, the CDRX is the main DRX mechanism during compression at 200 °C.

For AE sample, a small amount of $\{10\bar{1}2\}$ twins can also be activated at the beginning of deformation, as shown in Fig. 3(e). It has been reported that $\{10\bar{1}2\}$ twins can also influence the DRX process [21,23,36,37]. Thus, a grain with $\{10\bar{1}2\}$ twins in AE-200 °C-15% sample is also further analyzed in Fig. 10(b). Pole figure shows that both G3 and T31 exhibit scattered orientation distribution. It indicates that dislocation aggregation induces the continuous change in orientation. The point-to-point misorientation distribution indicates that the change in orientation largely destroys the structure of the twin boundary. The 86.3° relationship of the twin boundary is converted to be 67.4° relationship during compression at 200 °C. Moreover, profuse LAGBs also appear inside the twins (T31) besides in the parent grains (G3). The LAGBs in the twins will also be developed into the sub-structure and high-angle grain boundaries (HAGBs), resulting in formation of DRX grains. These characteristics are considered to be twin-induced DRX [20,23]. Figure 10(b) also shows that $\{10\bar{1}2\}$ twins can also promote the formation of sub-structure in parent grains and refine sub-structure. As shown in Fig. 10(b), some obvious

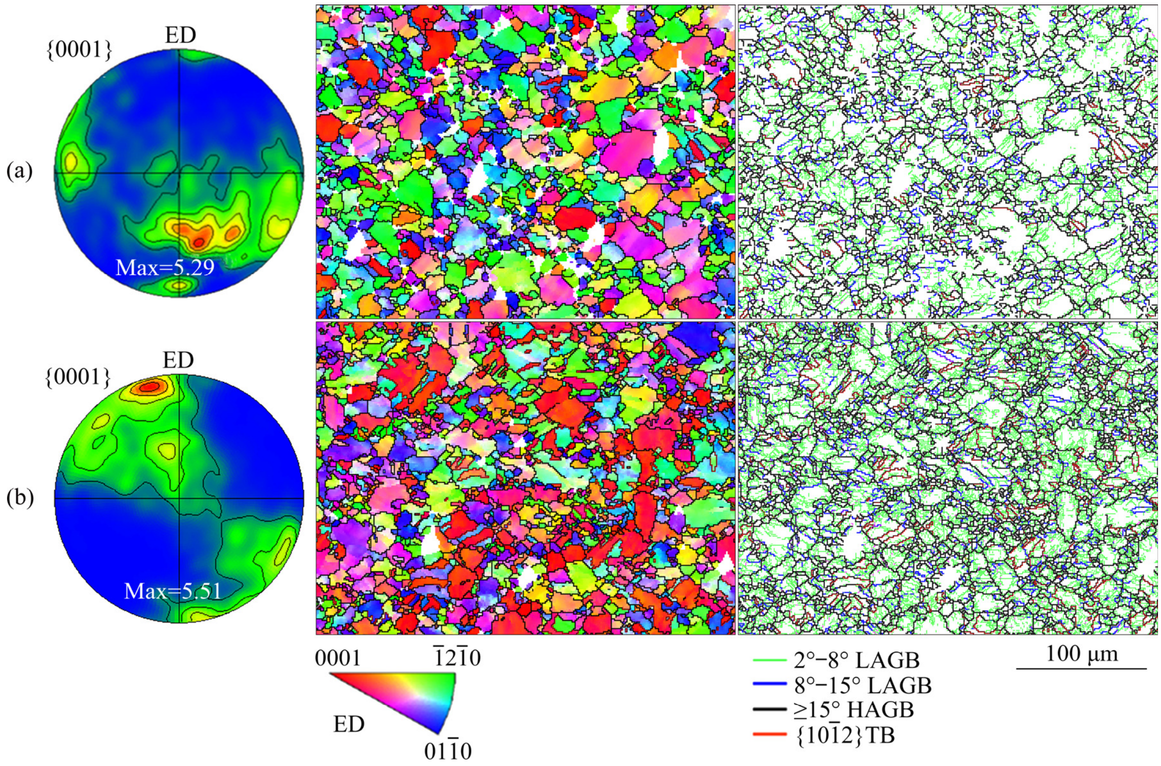

Fig. 9 EBSD data of various samples: (a) AE-200 °C-15%; (b) PT-200 °C-15%

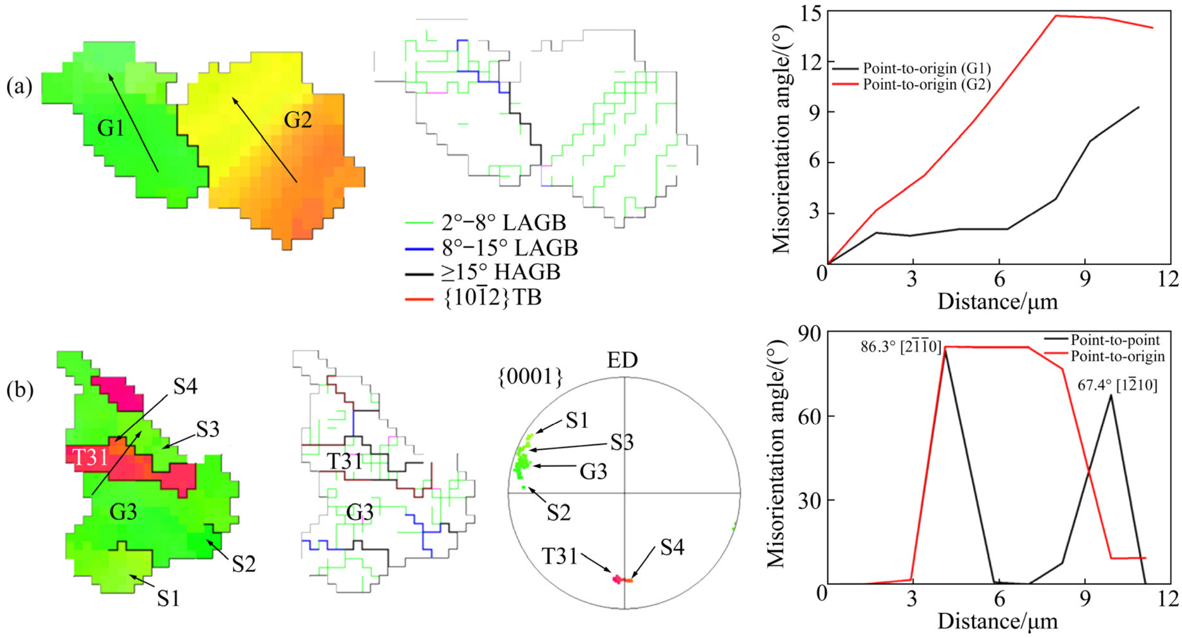

Fig. 10 Typical grains in AE-200 °C-15% sample: (a) Grains without twins; (b) Grain with {10$\bar{1}$2} twins (S*i* (*i*=1, 2, 3, ···) represents the sub-structures)

sub-structures have been formed (S1−S3). Moreover, a potential sub-structure can be found within Twin T31 (S4). Thus, it is considered that {10$\bar{1}$2} twins can promote the formation of sub-structures and subsequent DRX. However, for the AE sample, twin-related DRX is limited due to the low amount of twins.

In contrast, PT sample contains profuse initial twins and initial dislocations which will influence the DRX process. To evaluate the evolution of various types of grain boundaries during compression at 200 °C, the length of grain boundaries per area (*L*) is measured by EBSD data and is listed in Table 2. The subscript on the *L* indicates the type of grain boundary. Clearly, PT sample has higher L_{LAGB} and L_{twin} than AE sample with increasing compressive strain to 15% at 200 °C. The high density of boundaries in PT sample might promote DRX during subsequent compression at 200 °C.

Table 2 Lengths of various grain boundaries per area in various samples (μm^{-1})

Sample	$L_{\mathrm{LAGB(2°-8°)}}$	$L_{\mathrm{LAGB(>8°)}}$	L_{HAGB}	L_{twin}
AE	0.004	0.006	0.081	0.001
AE-200 °C-15%	0.118	0.021	0.088	0.007
PT	0.147	0.008	0.080	0.021
PT-200 °C-15%	0.179	0.025	0.112	0.015

Figure 11 shows three typical grains in PT-200 °C-15% sample. It is found that lots of LAGBs and {10$\bar{1}$2} twins can be found in PT-200 °C-15% sample. The intense distortion within grains resulting from initial LAGBs facilitates the formation of sub-structures during subsequent hot deformation. The initial twin boundaries via torsion are largely destroyed (see the Twin T11 in Grain G1) during compression, as shown in Figs. 11(a) and (b). Moreover, profuse LAGBs and sub-structures can be found in both parent grains and twins. Orientation change via dislocation aggregation in parent grain and twins leads to the destruction of twin boundaries. It indicates that the boundaries of {10$\bar{1}$2} twins can also act as effective barriers for slip to accumulate dislocations and therefore favor DRX [38]. Figure 11(c) illustrates the evolution of point-to-origin misorientation along the black arrows in the Grain G2 and Twin T31. It indicates that misorientations within initial grains and initial twins both exhibit a continuous increase. And a recrystallized grain can be found in Twin T31 (see the Grain R31). Clearly, there is intense distortion within the initial grains and initial twins, which is the CDRX feature [33,34]. Many LAGBs (>8°) are usually formed near the twin boundaries (see Grains G1, G2 and G3). Moreover, sub- structure and new recrystallized grain (R31) can be formed within initial twins (e.g. Twin T31). Thus, the initial twins effectively promote the formation of sub-structure and the subsequent CDRX process.

Figure 12 shows the EBSD data of the samples compressed to a strain of 50% at 200 °C. As compressive strain increases at 200 °C, *c*-axis of texture further rotates towards the ED. And single {0001} pole peak is formed in PT-200 °C-50% sample. Moreover, the $\{10\bar{1}2\}$ twins have disappeared completely, and a large number of fine

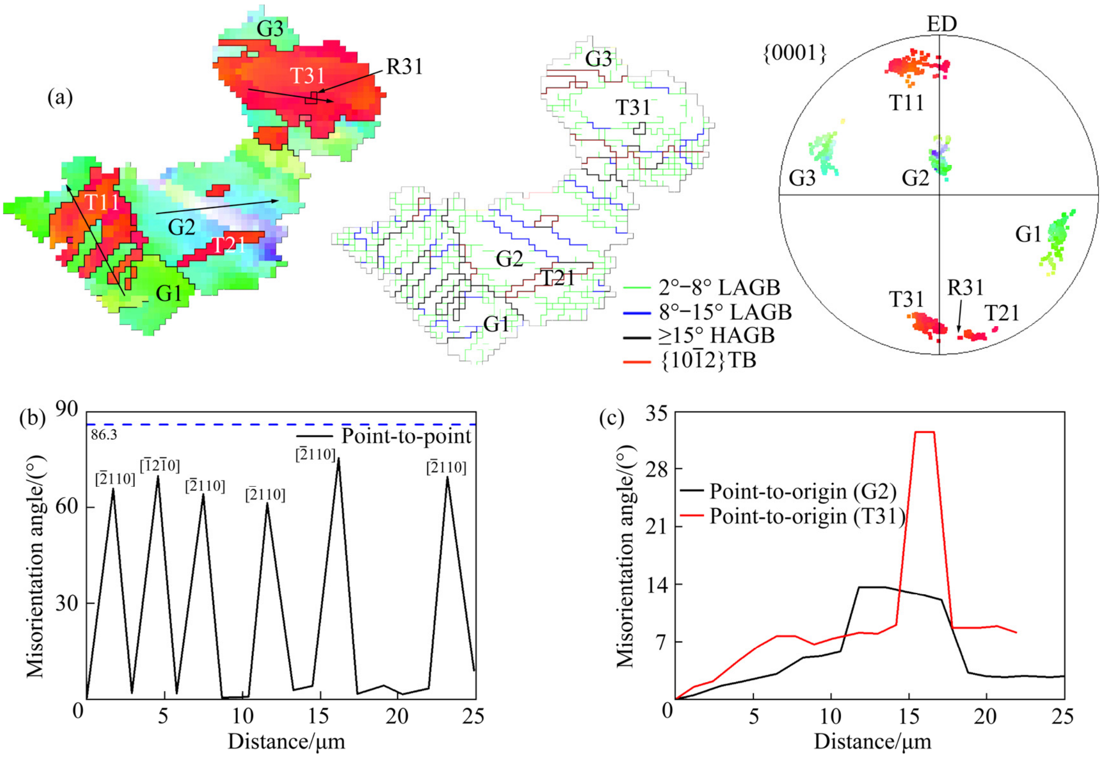

Fig. 11 Typical grains in PT-200 °C-15% sample: (a) EBSD maps and pole figure; (b) Misorientation measured along arrow directions in Grain G1; (c) Misorientation distribution measured along arrow directions in Grain G2 and Twin T31

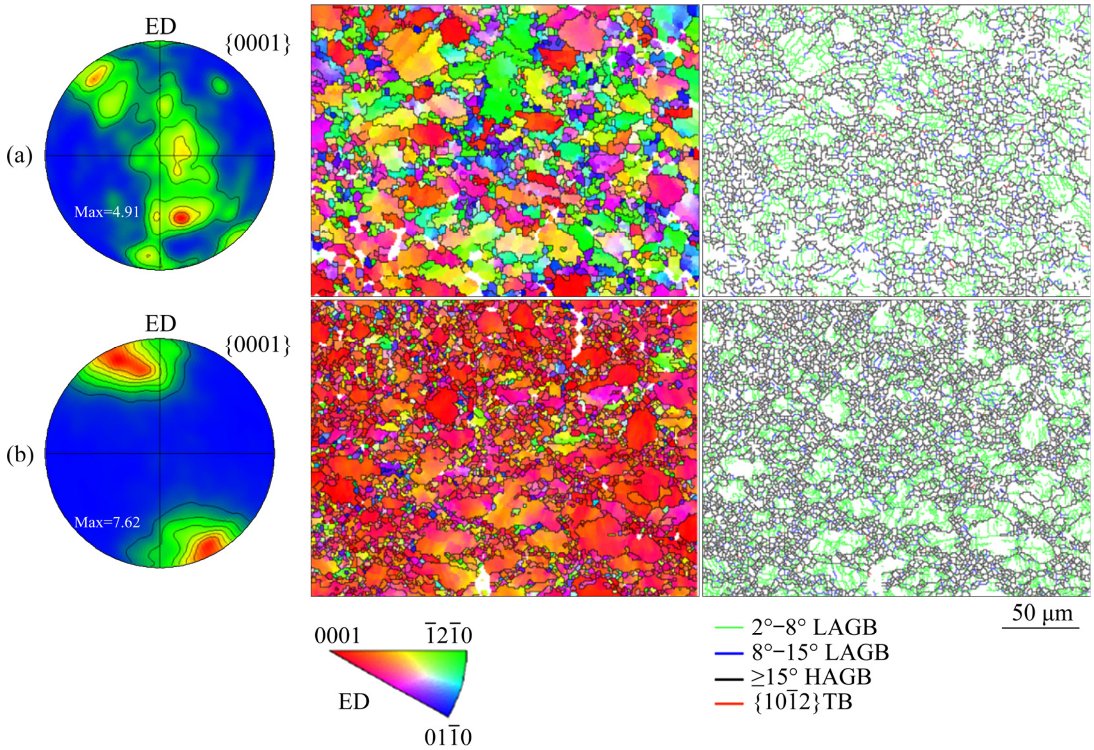

Fig. 12 EBSD data of various samples: (a) AE-200 °C-50%; (b) PT-200 °C-50%

recrystallized grains can be formed in PT-200 °C-50% and AE-200°C-50% samples. Size of fine DRX grains is usually lower than 10 μm. Thus, the grains whose size is smaller than 10 μm are considered to be DRX grains. Moreover, some coarse deformed grains contain profuse LAGBs to further perform the CDRX process. Based on EBSD data, the equivalent circle diameter of each grain can be measured by Channel 5 software. In this work, equivalent circle diameter of grains is measured to evaluate the evolution of grain size. The distribution of grain size for various samples is shown in Fig. 13. For AE sample, the grain size of most grains (65%) is smaller than 10 μm. However, their area fraction is only 13%. After being compressed by 50% at 200 °C, the number fraction of the grains which are smaller than 10 μm is increased to 89% and 97% for the AE-200°C-50% and PT-200°C-50% samples, respectively, as shown in Figs. 13(b) and (c). Moreover, it is also found that PT-200 °C-50% sample has a smaller DRX grain size than AE-200 °C-50% sample, as shown in Figs. 13(b) and (c). It might be attributed to the pre-torsion deformation, promoting the nucleation of DRX grains, as discussed above.

Figure 14 exhibits the EBSD data of the AE-300 °C-50% and the PT-300 °C-50% samples. It shows that the compression at 300 °C arouses similar texture evolution with the compression at 200 °C. Moreover, lots of LAGBs still exist in PT and AE samples during compression at 300 °C. It also proves that CDRX is still active during compression at 300 °C. It is also reported that the compression at 300 °C usually enhances the grain boundary migration. And the DRX mechanism will transform into DDRX [23,33]. As shown in Fig. 8, profuse bulges of grain boundaries are formed during compression at 300 °C, which is the characterization of DDRX. These bulges via grain boundary migration will develop into new fine

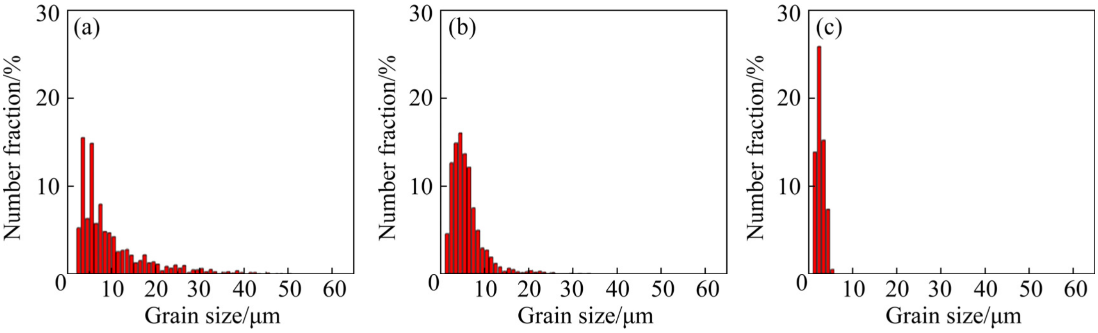

Fig. 13 Grain size (equivalent circle diameter) distributions from number fraction measurements: (a) AE sample; (b) AE-200 °C-50% sample; (c) PT-200 °C-50% sample

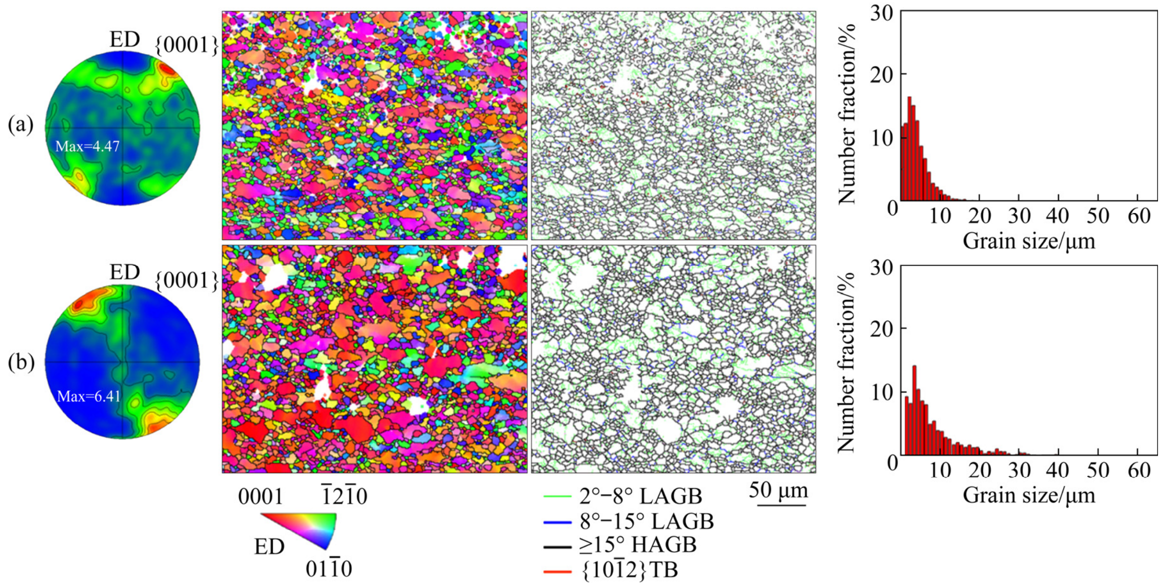

Fig. 14 {0001} pole figure, EBSD maps and grain size (equivalent circle diameter) distribution of various samples: (a) AE-300 °C-50%; (b) PT-300 °C-50%

DRX [39]. In addition, strong static recovery and static recrystallization at high temperature will change the subsequent DRX process. As shown in Figs. 3(g) and (h), both AE-300 °C-5% and PT-300 °C-5% samples exhibit an equiaxed microstructure and similar average grain size. It is inferred that initial dislocations and initial twins in PT sample have been largely consumed by static recovery and static recrystallization during holding time at 300 °C. According to the EBSD data, the $L_{\mathrm{LAGB}(2°-15°)}$ and L_{twin} are 0.040 and 0.001 μm^{-1} in AE-300 °C-5% sample, respectively, and 0.035 and 0.002 μm^{-1} in PT-300 °C-5% sample, respectively. Thus, the AE and PT samples contain almost equal $L_{\mathrm{LAGB}(2°-15°)}$ and L_{twin}. It can be seen that initial dislocations and twin structure via torsion will not affect the subsequent recrystallization process during compression at 300 °C. Thus, a similar DRX process is observed in the AE and PT samples, as shown in Fig. 8.

It is also found that the DRX grain size in AE-300 °C-50% sample is smaller than that in PT-300 °C-50% sample, as shown in Figs. 3 and 14. This may be related to different initial textures between the PT and AE sample [22,38,40]. It is mainly attributed to the influence of initial texture on the number of active slip modes during compression at 300 °C [31]. It is reported that DRX process can be accelerated when multiple slip modes (basal, prismatic and pyramidal slip) are activated. In contrast, when only single (basal) slip is favorable, DRX took place more slowly [22,31,41]. This is because the activity of multiple slip modes enhances the cross-slip of basal dislocations into non-basal planes [22]. For the AE sample with extrusion fiber texture, the cross-slip from basal to non-basal can be activated during compression at 300 °C. However, for PT sample with 70-ED and 40-ED textures, only single basal slip is favorable. It is considered that the texture of the AE sample is more conducive to the progress of DRX than that of the PT sample. As compressive strain increases at 300 °C, the *c*-axis of texture rotates towards ED, as shown in Fig. 14. It is inferred that as the deformation progresses, influence of initial texture on DRX might be weakened.

In this work, only the edge positions of twisted rods were investigated to analyze the effect of pre-torsion on the DRX behavior. It is considered that the edge position exhibits the largest change in microstructure during torsion. Here, it should also be emphasized that gradient microstructure can be formed in torsion-deformed samples [14]. It is reported that texture components, density of dislocations and amount of twins exhibit a gradient change on the cross-section of twisted rod. Thus, the DRX process might also be different on the cross-section of the rod. This will be investigated in further work.

4 Conclusions

(1) Pre-torsion deformation enhances the compressive yield strength of extruded AZ31 rod at less than 200 °C. As compressive temperature increases from RT to 200 °C, the increment in yield strength via torsion gradually decreases from 52 to 7 MPa. When compressed at 300 °C, torsion deformation reduces (by 14 MPa) the yield strength of the extruded rod.

(2) When compressed at 200 °C, flow softening behavior can be found owing to the initiation of DRX. It is found that the PT sample shows more rapid flow softening behavior than AE sample at 200 °C. It can be attributed to that the high density of dislocations and profuse $\{10\bar{1}2\}$ twins in the PT sample help to refine the sub-structure and accelerate the CDRX process.

(3) When compressed at 300 °C, compression flow curves of the PT and AE samples tend to be coincident. It can be attributed to that initial dislocations and twins in the PT sample are largely consumed by static recovery and static recrystallization during holding time at 300 °C. For compression at 300 °C, the discontinuous dynamic recrystallization was also enhanced. Moreover, textural change via torsion also affects the DRX process to a certain extent at 300 °C.

(4) Only the edge positions of twisted rods are investigated to analyze the effect of pre-torsion on the DRX behavior. However, gradient microstructure can be formed in torsion-deformed samples. Thus, the DRX process might also be different on the cross-section of the rod.

Acknowledgments

This work was supported by the National Natural Science Foundation of China (No. 51601154), and Southwest University Undergraduate Innovation Project (No. zsm2021026). The authors thank Hong-ju ZHANG from the Analytical & Testing Center, Southwest University for help with the EBSD experiments.

References

[1] SONG Jiang-feng, SHE Jia, CHEN Dao-lun, PAN Fu-sheng. Latest research advances on magnesium and magnesium alloys worldwide [J]. Journal of Magnesium and Alloys, 2020, 8(1): 1−41.

[2] MA Li-na, YANG Yan, ZHOU Gang, REN Feng-juan, DENG Hong-ju, WEI Guo-bing, PENG Xiao-dong. Effect of rolling reduction and annealing process on microstructure and corrosion behavior of LZ91 alloy sheet [J]. Transactions of Nonferrous Metals Society of China, 2020, 30: 1816−1825.

[3] CUI Chao, ZHANG Wen-cong, CHEN Wen-zhen, HE Jian, CHEN Xue-min, HOU Jia-bin. Microstructure, texture evolution and yield strength symmetry improvement of as-extruded ZK60 Mg alloy via multi-directional impact forging [J]. Journal of Magnesium and Alloys, 2022, 10(10): 2745−2760.

[4] DAI Shuai, WANG Feng, WANG Zhi, LIU Zheng, MAO Ping-li. Effect of Cu on microstructure, mechanical properties, and texture evolution of ZK60 alloy fabricated by hot extrusion−shearing process [J]. Transactions of Nonferrous Metals Society of China, 2020, 30: 1511−1523.

[5] FAN Ling-ling, ZHOU Ming-yang, GUO Yang-yang, ZHANG Yu-wen-xi, QUAN Gao-feng. Effect of ECAP process on liquid distribution of AZ80M alloy during semi-solid isothermal heat treatment [J]. Transactions of Nonferrous Metals Society of China, 2021, 31: 1599−1611.

[6] KONG T, KWAK B J, KIM J, LEE J H, PARK S H, KIM J H, MOON Y H, YOON H S, LEE T. Tailoring strength-ductility balance of caliber-rolled AZ31 Mg alloy through subsequent annealing [J]. Journal of Magnesium and Alloys, 2020, 8: 163−171.

[7] SIAHSARANI A, FARAJI G. Processing and characterization of AZ91 magnesium alloys via a novel severe plastic deformation method: Hydrostatic cyclic extrusion compression (HCEC) [J]. Transactions of Nonferrous Metals Society of China, 2021, 31: 1303−1321.

[8] SONG Bo, XIN Ren-long, ZHENG Xuan, CHEN Gang, LIU Qing. Activation of multiple twins by pre-tension and compression to enhance the strength of Mg−3Al−1Zn alloy plates [J]. Materials Science and Engineering A, 2015, 621: 100−104.

[9] YANG Qing-shan, JIANG Bin, SONG Bo, YU Zu-jian, HE De-wei, CHAI Yan-fu, ZHANG Jian-yue, PAN Fu-sheng. The effects of orientation control via tension-compression on microstructural evolution and mechanical behavior of AZ31 Mg alloy sheet [J]. Journal of Magnesium and Alloys, 2022, 10(2): 411−422.

[10] SONG Bo, DU Zhi-wen, YANG Qing-shan, GUO Ning, GUO Sheng-feng, YU Jin-cheng, XIN Ren-long. Effect of pre-rolling path on mechanical properties of rolled ZK60 alloys [J]. Transactions of Nonferrous Metals Society of China, 2021, 31: 1322−1338.

[11] ZHANG Hua, HUANG Guang-sheng, WANG Li-fei, ROVEN H J, XU Ze-bing, PAN Fu-sheng. Improved ductility of magnesium alloys by a simple shear process followed by annealing [J]. Scripta Materialia, 2013, 69: 49−52.

[12] SONG Bo, DU Zhi-wen, GUO Ning, YANG Qing-shan, WANG Fang, GUO Sheng-feng, XIN Ren-long. Effect of free-end torsion on microstructure and mechanical properties of AZ31 bars with square section [J]. Journal of Materials Science & Technology, 2021, 69: 20−31.

[13] SONG Bo, WANG Chun-peng, GUO Ning, PAN Hu-cheng, XIN Ren-long. Improving tensile and compressive properties of an extruded AZ91 rod by the combined use of torsion deformation and aging treatment [J]. Materials, 2017, 10: 280.

[14] SONG Bo, PAN Hu-cheng, CHAI Lin-jiang, GUO Ning, ZHAO Huai-zhi, XIN Ren-long. Evolution of gradient microstructure in an extruded AZ31 rod during torsion and annealing and its effects on mechanical properties [J]. Materials Science and Engineering A, 2017, 689: 78−88.

[15] SONG Bo, SHU Xiao-gang, PAN Hu-cheng, LI Guo-qiang, GUO Ning, LIU Ting-ting, CHAI Lin-jiang, XIN Ren-long. Influence of torsion route on the microstructure and mechanical properties of extruded AZ31 rods [J]. Advanced Engineering Materials, 2017, 19: 1700267.

[16] SONG Bo, GUO Ning, XIN Ren-long, PAN Hu-cheng, GUO Chang-fa. Strengthening and toughening of extruded magnesium alloy rods by combining pre-torsion deformation with subsequent annealing [J]. Materials Science and Engineering A, 2016, 650: 300−304.

[17] HU Jia-qi, GAO Hong, MENG Yu-xian, ZHANG Zhe, GAO Li-lan. Effects of free-end torsion on the microstructure evolution and fatigue properties in an extruded AZ31 rod [J]. Materials Science and Engineering A, 2018, 726: 215−222.

[18] TAM K J, VAUGHAN M W, SHEN L M, KNEZEVIC M, KARAMAN I, PROUST G. Modelling the temperature and texture effects on the deformation mechanisms of magnesium alloy AZ31 [J]. International Journal of Mechanical Sciences, 2020, 182: 105727.

[19] DU Yu-zhou, LIU Dong-jie, GE Yan-feng, JIANG Bai-ling. Effects of deformation parameters on microstructure and texture of Mg−Zn−Ce alloy [J]. Transactions of Nonferrous Metals Society of China, 2020, 30: 2658−2668.

[20] LI Zi-han, ZHOU Guo-wei, LI Da-yong, WANG Hua-miao, TANG Wei-qin, PENG Ying-hong, ZUROB H S, WU Pei-dong. Crystal plasticity based modeling of grain boundary sliding in magnesium alloy AZ31B sheet [J]. Transactions of Nonferrous Metals Society of China, 2021, 31: 138−155.

[21] POPOVA E, BRAHME A P, STARASELSKI Y, AGNEW S R, MISHRA R K, INAL K. Effect of extension $\{10\bar{1}\bar{2}\}$ twins on texture evolution at elevated temperature deformation accompanied by dynamic recrystallization [J]. Materials & Design, 2016, 96: 446−457.

[22] DEL VALLE J A, RUANO O A. Influence of texture on dynamic recrystallization and deformation mechanisms in rolled or ECAPed AZ31 magnesium alloy [J]. Materials Science and Engineering A, 2008, 487: 473−480.

[23] ZHANG Hua, BAI Xiao-qing, HOU Min-jian, WANG Li-fei, ZHANG Qiang, FAN Jian-feng, WU Yu-cheng, DONG Hong-biao, XU Bing-she. Enhancing compressive mechanical properties of rolled AZ31 Mg alloy plates by

pre-compression [J]. Materials Science and Engineering A, 2020, 772: 138686.

[24] HOU Cai-hong, YE Zhi-song, QI Fu-gang, WANG Qing, LI Lian-hui, OUYANG Xiao-ping, ZHAO Nie. Effect of Al addition on microstructure and mechanical properties of Mg−Zn−Sn−Mn alloy [J]. Transactions of Nonferrous Metals Society of China, 2021, 31:1951−1968.

[25] HONG S G, PARK S H, LEE C S. Role of $\{10\bar{1}2\}$ twinning characteristics in the deformation behavior of a polycrystalline magnesium alloy [J]. Acta Materialia, 2010, 58: 5873−5885.

[26] DU Zhi-wen, SONG Bo, GUO Ning, LIU Ting-ting, GUO Sheng-feng, XIN Ren-long. Revealing the texture evolution and compressive anisotropy in free-end twisted AZ31 rods [J]. Journal of Materials Engineering and Performance, 2021, 30: 1157−1166.

[27] BISWAS S, BEAUSIR B, TOTH L S, SUWAS S. Evolution of texture and microstructure during hot torsion of a magnesium alloy [J]. Acta Materialia, 2013, 61: 5263−5277.

[28] RUI Shao-shi, HAN Qi-nan, WANG Xue, LI Shan-lin, MA Xian-feng, SU Yue, CAI Zhi-peng, DU Dong, SHI Hui-ji. Correlations between two EBSD-based metrics Kernel Average Misorientation and Image Quality on indicating dislocations of near-failure low alloy steels induced by tensile and cyclic deformations [J]. Materials Today Communications, 2021, 27: 102445.

[29] WU P D, GUO X Q, QIAO H, AGNEW S R, LLOYD D J, EMBURY J D. On the rapid hardening and exhaustion of twinning in magnesium alloy [J]. Acta Materialia, 2017, 122: 369−377.

[30] BUSK R S. Magnesium and its alloys [M]. New York: Myer Kutz Associates, Inc, 2001.

[31] KAIBYSHEV R, SOKOLOV B, GALIYEV A. The influence of crystallographic texture on dynamic recrystallization [J].Textures and Microstructures, 1999, 32: 47−63.

[32] SONG Bo, XIN Ren-long, CHEN Gang, ZHANG Xi-yan, LIU Qing. Improving tensile and compressive properties of magnesium alloy plates by pre-cold rolling [J]. Scripta Materialia, 2012, 66: 1061−1064.

[33] PARK C H, OH C S, KIM S. Dynamic recrystallization of the H- and O-tempered Mg AZ31 sheets at elevated temperatures [J]. Materials Science and Engineering A, 2012, 542: 127−139.

[34] XU S W, KAMADO S, MATSUMOTO N, HONMA T, KOJIMA Y. Recrystallization mechanism of as-cast AZ91 magnesium alloy during hot compressive deformation [J]. Materials Science and Engineering A, 2009, 527: 52−60.

[35] GALIYEV A, KAIBYSHEV R, GOTTSTEIN G. Correlation of plastic deformation and dynamic recrystallization in magnesium alloy ZK60 [J]. Acta Materialia, 2001, 49: 1199−1207.

[36] ZHANG Hua, YANG Mu-xuan, HOU Min-jian, WANG Li-fei, ZHANG Qiang, FAN Jian-feng, LI Wei-guo, DONG Hong-biao, LIU Sheng-ming, XU Bing-she. Effect of pre-existing $\{101\bar{2}\}$ extension twins on mechanical properties, microstructure evolution and dynamic recrystallization of AZ31 Mg alloy during uniaxial compression [J]. Materials Science and Engineering A, 2019, 744: 456−470.

[37] MA Q, LI B, MARIN E B, HORSTEMEYER S J. Twinning-induced dynamic recrystallization in a magnesium alloy extruded at 450 °C [J]. Scripta Materialia, 2011, 65: 823−826.

[38] GAO P, ZHU S Q, AN X H, XU S Q, RUAN D, CHEN C, YAN H G, RINGER S P, LIAO X Z. Effect of sample orientation and initial microstructures on the dynamic recrystallization of a magnesium alloy [J]. Materials Science and Engineering A, 2017, 691: 150−154.

[39] MARTIN É, JONAS J J. Evolution of microstructure and microtexture during the hot deformation of Mg−3%Al [J]. Acta Materialia, 2010, 58: 4253−4266.

[40] HAO Mei-juan, CHENG Wei-li, WANG Li-fei, MOSTAED E, BIAN Li-ping, WANG Hong-xia, NIU Xiao-feng. Texture evolution induced by twinning and dynamic recrystallization in dilute Mg−1Sn−1Zn−1Al alloy during hot compression [J]. Journal of Magnesium and Alloys, 2020, 8: 899−909.

[41] DUDAMELL N V, ULACIA I, GÁLVEZ F, YI S, BOHLEN J, LETZIG D, HURTADO I, PÉREZ-PRADO M T. Influence of texture on the recrystallization mechanisms in an AZ31 Mg sheet alloy at dynamic rates [J]. Materials Science and Engineering A, 2012, 532: 528−535.

自由端扭转对 AZ31 挤压棒不同温度下压缩行为的影响

吴 凡，王 猛，杜治文，石若兰，尚 琦，刘婷婷，郭 宁，郭胜锋，宋 波

西南大学 材料与能源学院，重庆 400715

摘　要：研究自由端扭转对 AZ31 挤压棒不同温度下压缩行为的影响。预扭转会在基体中产生高密度位错和大量的 $\{10\bar{1}2\}$ 孪晶，从而大大提升室温和 100 ℃的压缩屈服强度。然而，随着温度的升高，预扭转产生的硬化效果逐渐减弱。当压缩温度达到 300 ℃时，预扭转降低了压缩屈服强度。此外，扭转产生的初始位错和孪晶有助于细化亚结构，加快 200 ℃压缩过程中的连续动态再结晶。因此，在 200 ℃下，扭转试样比挤压试样表现出更快的流变软化行为。当在 300 ℃时压缩，扭转引入的孪晶和位错在保温时间内基本被消除，不连续动态再结晶得到增强。结果表明，在 300 ℃时，扭转试样和挤压试样的压缩曲线趋于一致。对相关机制进行了详细讨论。

关键词：镁合金；自由端扭转；压缩行为；动态再结晶；热变形；孪晶；位错

(Edited by Xiang-qun LI)